

# Nonlocal optical second harmonic generation from centrosymmetric birefringent crystals: the case of muscovite mica

Annunziata Savoia, Marco Siano, Domenico Paparo,\* and Lorenzo Marrucci

*CNR-SPIN and Dipartimento di Scienze Fisiche, Università di Napoli "Federico II,"  
Complesso Università di Monte Sant'Angelo, via Cintia, 80126 Napoli, Italy*

*\*Corresponding author: paparo@na.infn.it*

Received September 2, 2010; revised January 4, 2011; accepted January 7, 2011;  
posted January 12, 2011 (Doc. ID 134452); published March 10, 2011

We present a detailed study of the optical second harmonic (SH) generated in samples of centrosymmetric muscovite mica. Samples with thicknesses ranging from 30 to 300  $\mu\text{m}$  have been investigated in a transmission normal-incidence geometry. We found a strong dependence of the polarization-dependent SH signal on the sample thickness. In particular, in some of the thickest samples, the SH signal is strongly enhanced. This signal amplification is not monotonically increased with thickness, but it varies erratically. These findings show that under the present experimental conditions, quadrupolar bulk second harmonic generation in mica becomes dominant on the SH generated from the surfaces. The large variability of the SH signal with the variation in thickness is then ascribed to partial optical phase-matching effects, controlled by the mica birefringence. In order to corroborate this hypothesis, a detailed theoretical model accounting for the nonlocal response and anisotropy of a generic birefringent crystal has been developed. The predictions of our model are found to be in excellent agreement with the experimental data. © 2011 Optical Society of America

*OCIS codes:* 000.2190, 190.0190, 190.4720, 310.0310, 310.6860.

## 1. INTRODUCTION

Muscovite mica is a mineral belonging to the group of phyllosilicates, widely used as substrate for technological and biological applications because of its cleavage properties [1–6]. These properties allow one to easily produce atomically flat surfaces over an area of several squared centimeters, thus providing ideal substrates for the deposition of materials whose roughness needs to be controlled at atomic scale. In addition, mica is transparent in both the visible and infrared spectral regions, and it is a centrosymmetric crystal.

The latter property renders mica an ideal substrate when second harmonic generation (SHG) is used for investigating ultrathin films or monolayers of molecular adsorbates. SHG is based on a second-order optical phenomenon that consists of the frequency doubling of some of the incident photons (at the fundamental frequency) during their interaction with the material. The frequency-doubled photons are typically seen in the reflected or transmitted light. Therefore an experimental reflection or transmission geometry may generally be used. The surface sensitivity of SHG arises because, under dipole approximation, the second-order nonlinear susceptibility characterizing the SHG response of the material vanishes in the bulk of centrosymmetric media. In contrast, where the inversion symmetry is broken, such as at a surface or interface, a relatively strong response is obtained, as demonstrated in a large variety of physical systems [7–12]. This renders SHG extremely sensitive to the interface, much more so than normal linear optical spectroscopies. However, beyond the dipole approximation, nonlocal higher order effects can also lead to a significant SHG in the bulk of centrosymmetric materials [13–15]. In centrosymmetric materials, this volume process is much less efficient than in surface SHG, but it integrates

on a larger fraction of the material. Therefore, under specific experimental conditions, it can exceed and eventually hide the second harmonic (SH) signal generated from the surface. When this happens, the power of this technique as a surface probe is drastically reduced. To minimize these bulk contributions, often a reflection geometry is used [16]. However, there are experiments, as in SHG microscopy, where a transmission geometry cannot be avoided. In this case, a detailed knowledge of the nonlocal contribution to SHG in mica would be highly desirable in order to select alternative strategies for maximizing the signal-to-noise ratio or for an effective subtraction of the substrate background. So far, a detailed experimental investigation of the nonlocal SHG response in mica has never been reported in literature. In Ref. [17], the results of some experiments of SHG from mica in a transmission geometry are reported. Because mica is centrosymmetric, the observed SH signal was assumed to originate from the crystal surfaces, but this assumption was not supported by any experimental evidence. In a later paper, the same author, together with others, succeeded in isolating the SHG contribution from only the back surface of a mica crystal by using a suitable wavelength, which allows suppression of, through absorption, the SH signal generated in the volume [18]. However, the issue of discriminating between surface and bulk SHG in mica remains open.

An important experimental test for discriminating between surface and bulk SHG is based on verifying the dependence of the SH signal on the sample thickness, but this analysis is missing in the aforementioned Ref. [17]. Therefore, aimed at bridging this gap, in this work we have performed a detailed experimental study of polarization-dependent SHG in mica

samples with different thicknesses and in a transmission geometry.

In order to model our experimental results, we have developed a detailed theory of nonlocal SHG in centrosymmetric materials. Because mica is a birefringent crystal, our derivation has tackled the additional complication of including birefringence.

We stress that our theoretical analysis is actually independent of the specific case of mica, and it is applicable to any centrosymmetric birefringent crystal, including dichroic crystals, although with some additional restriction, as explained in the following. In particular, we consider the general case of a crystal whose principal dielectric axis does not lie in a plane parallel to the crystal input face. To our knowledge, a general theory describing nonlocal SHG in birefringent centrosymmetric crystals and in a transmission geometry has never been reported in the literature. We quote here the paper by Omote *et al.* [19], in which an analogous theoretical analysis is presented for birefringent centrosymmetric crystals, but for a geometry in reflection and for the case of a uniaxial crystal whose axis is perpendicular or parallel to the crystal input face. As we will show in the following, in a transmission geometry, phase-matching effects play a crucial role and lead to a dramatic dependence of the SH signal with thickness and birefringence, which was not explicitly analyzed in Ref. [19]. For all these reasons, in the next section and in Appendix A, we present our theory in detail.

## 2. THEORY

In this section, we describe the theory of nonlocal SHG in birefringent centrosymmetric crystals in a transmission normal-incidence geometry.

### A. Nonlinear Nonlocal Constitutive Equations

SHG is a nonlinear optical process in which the response of a material, characterized by the electric polarization  $\mathbf{P}(\mathbf{k}, \omega)$  in the Fourier-transform space, acquires a component  $\mathbf{P}_{2\omega}^{(2)}(\mathbf{k})$  quadratic in the electric field of the input wave, called second-order nonlinear polarization. In general, the value of  $\mathbf{P}(\mathbf{k}, \omega)$  depends on the value of the field in some region of the material. Therefore, assuming only homogeneity of the medium, the general constitutive equation, accounting for spatial and temporal dispersion, at the second order in the optical field is written

$$\begin{aligned} P_j(\mathbf{k}, \omega) &= P_{j,\omega}^{(1)}(\mathbf{k}) + P_{j,2\omega}^{(2)}(\mathbf{k}) \\ &= \epsilon_0 \tilde{\chi}_{jh}^{(1)}(\mathbf{k}, \omega) E_h(\mathbf{k}, \omega) + \int \tilde{\chi}_{jhl}^{(2)}(\mathbf{k}', \mathbf{k}'', \omega', \omega'') \\ &\quad \times E_h(\mathbf{k}', \omega') E_l(\mathbf{k}'', \omega'') \delta(\omega - \omega' - \omega'') \\ &\quad \times \delta(\mathbf{k} - \mathbf{k}' - \mathbf{k}'') d^3\mathbf{k}' d^3\mathbf{k}'' d\omega' d\omega'', \end{aligned} \quad (1)$$

where  $E_h$  are the electrical field components for a monochromatic input field,  $\tilde{\chi}^{(1)}$  is the linear susceptibility tensor,  $\tilde{\chi}^{(2)}$  is the second-order nonlinear susceptibility tensor, and Dirac- $\delta$  functions are used. Here, and in the following, the Einsteinian sum rule on repeated indices is used unless otherwise specified.

Usually the spatial dispersion is weak, and the functions  $\tilde{\chi}_{jh}^{(1)}(\mathbf{k}, \omega)$  and  $\tilde{\chi}_{jhl}^{(2)}(\mathbf{k}', \mathbf{k}'', \omega', \omega'')$  can be hence expanded in the power series up to the first order in the variable  $\mathbf{k}$ . We thus obtain

$$\tilde{\chi}_{jh}^{(1)}(\mathbf{k}, \omega) = \chi_{jh}^{(1)}(\omega) + g_{jhl}(\omega) k_l, \quad (2)$$

$$\begin{aligned} \tilde{\chi}_{jhl}^{(2)}(\mathbf{k}', \mathbf{k}'', \omega', \omega'') &= \chi_{jhl}^{(2)}(\omega', \omega'') + \gamma_{jhlq}(\omega', \omega'') k'_q \\ &\quad + \bar{\gamma}_{jhlq}(\omega', \omega'') k''_q, \end{aligned} \quad (3)$$

where the following quantities have been introduced:

$$\chi_{jh}^{(1)}(\omega) = \tilde{\chi}_{jh}^{(1)}(0, \omega), \quad (4)$$

$$\chi_{jhl}^{(2)}(\omega', \omega'') = \tilde{\chi}_{jhl}^{(2)}(0, 0, \omega', \omega''), \quad (5)$$

$$g_{jhl}(\omega) = \partial \tilde{\chi}_{jh}^{(1)} / \partial k_l |_{\mathbf{k}=0}, \quad (6)$$

$$\gamma_{jhlq}(\omega', \omega'') = \partial \tilde{\chi}_{jhl}^{(2)} / \partial k'_q |_{\mathbf{k}'=0, \mathbf{k}''=0}, \quad (7)$$

$$\bar{\gamma}_{jhlq}(\omega', \omega'') = \partial \tilde{\chi}_{jhl}^{(2)} / \partial k''_q |_{\mathbf{k}'=0, \mathbf{k}''=0}. \quad (8)$$

The latter functions satisfy the following symmetry relations

$$\chi_{jhl}^{(2)}(\omega', \omega'') = \chi_{jih}^{(2)}(\omega'', \omega'), \quad (9)$$

$$\gamma_{jhlq}(\omega', \omega'') = \bar{\gamma}_{jihq}(\omega'', \omega'). \quad (10)$$

The function  $g_{jhl}(\omega)$  accounts for the chirality of the medium and vanishes in centrosymmetric media (it will be neglected in the following).

In real space, Eq. (1) is rewritten as

$$\begin{aligned} P_j(\mathbf{r}, \omega) &= \epsilon_0 \chi_{jh}^{(1)}(\omega) E_h(\mathbf{r}, \omega) \\ &\quad + \int d\omega' d\omega'' \chi_{jhl}^{(2)}(\omega', \omega'') E_h(\mathbf{r}, \omega') E_l(\mathbf{r}, \omega'') \delta(\omega - \omega' - \omega'') \\ &\quad - i \int d\omega' d\omega'' \gamma_{jhlq}(\omega', \omega'') E_l(\mathbf{r}, \omega'') \\ &\quad \times \frac{\partial}{\partial x_q} E_h(\mathbf{r}, \omega') \delta(\omega - \omega' - \omega'') \\ &\quad - i \int d\omega' d\omega'' \bar{\gamma}_{jhlq}(\omega', \omega'') E_h(\mathbf{r}, \omega') \\ &\quad \times \frac{\partial}{\partial x_q} E_l(\mathbf{r}, \omega'') \delta(\omega - \omega' - \omega''). \end{aligned} \quad (11)$$

If a monochromatic wave at frequency  $\bar{\omega}$  impinges on the medium, the nonlinear interaction described by Eq. (11) generates optical radiation at  $2\bar{\omega}$ . In order to consider all the possible couplings between these two optical components, it is useful to write the optical field in the following form:

$$\begin{aligned} E_j(\mathbf{r}, \omega) &= E_{j,\bar{\omega}}(\mathbf{r}) \delta(\omega - \bar{\omega}) + E_{j,\bar{\omega}}^*(\mathbf{r}) \delta(\omega + \bar{\omega}) \\ &\quad + E_{j,2\bar{\omega}}(\mathbf{r}) \delta(\omega - 2\bar{\omega}) + E_{j,2\bar{\omega}}^*(\mathbf{r}) \delta(\omega + 2\bar{\omega}), \end{aligned} \quad (12)$$

where the symbol  $*$  indicates complex conjugation. Consequently, the medium nonlinear polarization is written

$$P_j(\mathbf{r}, \omega) = P_{j,\bar{\omega}}(\mathbf{r})\delta(\omega - \bar{\omega}) + P_{j,\bar{\omega}}^*(\mathbf{r})\delta(\omega + \bar{\omega}) \\ + P_{j,2\bar{\omega}}(\mathbf{r})\delta(\omega - 2\bar{\omega}) + P_{j,2\bar{\omega}}^*(\mathbf{r})\delta(\omega + 2\bar{\omega}), \quad (13)$$

where

$$P_{j,\bar{\omega}}(\mathbf{r}) = \epsilon_0 \chi_{jh}^{(1)}(\bar{\omega}) E_{h,\bar{\omega}}(\mathbf{r}), \quad (14)$$

$$P_{j,2\bar{\omega}}(\mathbf{r}) = \epsilon_0 \chi_{jh}^{(1)}(2\bar{\omega}) E_{h,2\bar{\omega}}(\mathbf{r}) + \chi_{jhl}^{(2)}(\bar{\omega}, \bar{\omega}) E_{h,\bar{\omega}}(\mathbf{r}) E_{l,\bar{\omega}}(\mathbf{r}) \\ - i\gamma_{jhlq}(\bar{\omega}, \bar{\omega}) E_{l,\bar{\omega}}(\mathbf{r}) \frac{\partial}{\partial x_q} E_{h,\bar{\omega}}(\mathbf{r}) \\ - i\bar{\gamma}_{jhlq}(\bar{\omega}, \bar{\omega}) E_{h,\bar{\omega}}(\mathbf{r}) \frac{\partial}{\partial x_q} E_{l,\bar{\omega}}(\mathbf{r}). \quad (15)$$

Equation (14) is obtained under the pump nondepletion approximation, meaning that the effect of the weak SH field on the strong pump has been neglected [20].

Based on symmetry arguments, it is straightforward to show that in the volume of centrosymmetric materials,  $\chi_{jhl}^{(2)}(\bar{\omega}, \bar{\omega})$  vanishes [8]. In these materials, it is different from zero only at surfaces where the inversion symmetry is naturally broken. The only contribution to SHG from the bulk of the centrosymmetric materials derives from the nonlocality of the nonlinear response accounted for by the functions  $\gamma_{jhlq}$  and  $\bar{\gamma}_{jhlq}$ . In the following, it is assumed that the SH signal generated in the bulk is much stronger than the surface SHG. Therefore, all the contributions to SHG deriving from  $\chi_{jhl}^{(2)}(\bar{\omega}, \bar{\omega})$  will be neglected. By applying the intrinsic symmetry to Eq. (13), the second-order nonlocal response is written

$$P_{j,2\bar{\omega}}(\mathbf{r}) = \epsilon_0 \chi_{jh}^{(1)}(2\bar{\omega}) E_{h,2\bar{\omega}}(\mathbf{r}) + P_{j,2\bar{\omega}}^{\text{NL}}(\mathbf{r}), \quad (16)$$

where

$$P_{j,2\bar{\omega}}^{\text{NL}}(\mathbf{r}) = \Gamma_{jhlq}(\bar{\omega}, \bar{\omega}) E_{h,\bar{\omega}}(\mathbf{r}) \frac{\partial}{\partial x_q} E_{l,\bar{\omega}}(\mathbf{r}), \quad (17)$$

$$\Gamma_{jhlq}(\bar{\omega}, \bar{\omega}) = -2i\gamma_{jhlq}(\bar{\omega}, \bar{\omega}) = -2i\bar{\gamma}_{jhlq}(\bar{\omega}, \bar{\omega}). \quad (18)$$

## B. Nonlocal Second Harmonic Radiation Generated in Centrosymmetric Anisotropic Materials

In this section, a general analytical expression for the SHG generated in the bulk of centrosymmetric anisotropic materials will be derived. Let an anisotropic centrosymmetric crystal occupy a region of space in the laboratory frame extending from  $z = 0$  to  $z = d$ . The crystal surfaces are parallel to the plane  $x$ - $y$  (see Fig. 1). The input beam is assumed to impinge on the face  $z = 0$  of the sample at normal incidence. To simplify the notation, here and in the following, the input beam frequency  $\bar{\omega}$  will be indicated as  $\omega$ . In the following, we will limit our treatment to the case of a plane wave, which can be analytically solved.

Based on Eq. (12) for the optical field and Eq. (13) for the polarization that acts as source for the Maxwell equations, the SH radiation is obtained by solving the following coupled equations:

$$\frac{d^2}{dz^2} E_{j,\omega}(z) - \delta_{jz} \frac{d^2}{dz^2} E_{z,\omega}(z) + \mu_0 \omega^2 \epsilon_{jh}(\omega) E_{h,\omega}(z) = 0, \quad (19)$$

$$\frac{d^2}{dz^2} E_{j,2\omega}(z) - \delta_{jz} \frac{d^2}{dz^2} E_{z,2\omega}(z) + 4\mu_0 \omega^2 \epsilon_{jh}(2\omega) E_{j,2\omega}(z) \\ = -4\mu_0 \omega^2 P_{j,2\omega}^{\text{NL}}(z), \quad (20)$$

where the dielectric tensor  $\epsilon_{jh} = \epsilon_0(\delta_{jh} + \chi_{jh}^{(1)})$  has been introduced and  $\delta_{jh}$  is the Kronecker symbol. It is worth noting that in Eq. (19), there is no coupling between the pump wave at  $\omega$  and the SH wave at  $2\omega$ . This is a consequence of the pump nondepletion approximation.

Equations (19) and (20) imply that the  $z$  component of the field can be expressed in terms of  $x$  and  $y$  components as follows:

$$E_{z,\omega} = - \sum_{j=x,y} \frac{\epsilon_{zj}}{\epsilon_{zz}} E_{j,\omega}, \quad (21)$$

$$E_{z,2\omega} = - \sum_{j=x,y} \frac{\epsilon_{zj}}{\epsilon_{zz}} E_{j,2\omega} - \frac{1}{\epsilon_{zz}} P_{z,2\omega}^{\text{NL}}. \quad (22)$$

Equations (21) and (22) may be used to reduce the initial three equations for the optical field to the following two:

$$\frac{d^2}{dz^2} E_{j,\omega}(z) + \mu_0 \omega^2 \bar{\epsilon}_{jh}(\omega) E_{h,\omega}(z) = 0, \quad (23)$$

$$\frac{d^2}{dz^2} E_{j,2\omega}(z) + 4\mu_0 \omega^2 \bar{\epsilon}_{jh}(2\omega) E_{j,2\omega}(z) = -4\mu_0 \omega^2 \bar{\Gamma}_{jhl} E_{h,\omega} \frac{d}{dz} E_{l,\omega}, \quad (24)$$

where now  $j, h, l = x, y$ , and the following two-dimensional tensors have been introduced:

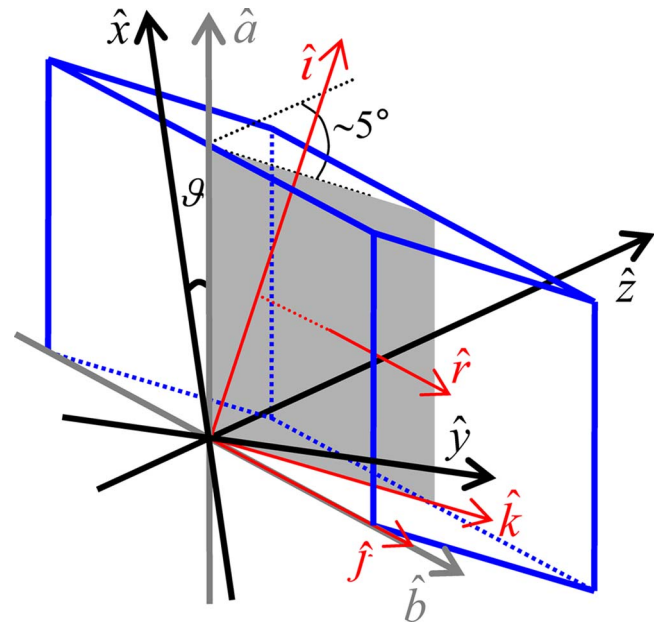


Fig. 1. (Color online) Axis orientation for the laboratory reference frame  $x\hat{y}z$  and crystal reference frame  $i\hat{j}k$ . Axes  $\hat{a}$  and  $\hat{b}$  represent the projection of the dielectric axis  $\hat{i}$  and  $\hat{j}$  on the cleavage plane parallel to the  $\hat{x}\hat{y}$  plane. The tensor  $\bar{\epsilon}_{ij}$  is diagonal respect to these axes (see text).  $\vartheta$  is the angle formed between axis  $\hat{x}$  and  $\hat{a}$ . For mica, the  $\hat{k}$  axis forms a small  $5^\circ$  angle with the  $\hat{z}$  axis (this angle has been exaggerated in figure for clarity) and the shadowed rectangle represents the intersection between the glide plane and crystal cell itself, whereas the  $\hat{r}$  axis is the twofold axis.

$$\bar{\epsilon}_{jh} = \epsilon_{jh} - \frac{\epsilon_{jz}\epsilon_{zh}}{\epsilon_{zz}}, \quad (25)$$

$$\begin{aligned} \bar{\Gamma}_{jhl} &= \Gamma_{jhlz} - \frac{\epsilon_{jz}}{\epsilon_{zz}}\Gamma_{zhlz} - \frac{\epsilon_{zl}}{\epsilon_{zz}}\Gamma_{jhzz} - \frac{\epsilon_{zh}}{\epsilon_{zz}}\Gamma_{jz lz} + \frac{\epsilon_{jz}\epsilon_{zl}}{\epsilon_{zz}^2}\Gamma_{zhzz} \\ &+ \frac{\epsilon_{jz}\epsilon_{zh}}{\epsilon_{zz}^2}\Gamma_{zzlz} + \frac{\epsilon_{zl}\epsilon_{zh}}{\epsilon_{zz}^2}\Gamma_{jzzz} - \frac{\epsilon_{jz}\epsilon_{zh}\epsilon_{zl}}{\epsilon_{zz}^3}\Gamma_{zzzz}. \end{aligned} \quad (26)$$

Note that the tensor  $\bar{\epsilon}_{jh}$  is symmetric as the original dielectric tensor. Therefore, there exist two orthogonal axes  $a$ - $b$  in the  $x$ - $y$  plane, which allow us to diagonalize it (see Fig. 1). We assume that these two axes are the same for both the fundamental and the SH frequencies, only slightly reducing the generality of our theory. A similar limitation instead must be introduced if we want to consider dichroic crystals, too. In this case, our approach is still valid if we can assume that the real and imaginary parts of the  $\bar{\epsilon}_{jh}$  tensor may be diagonalized with the same pair of axis.

In the  $abz$  reference system, it is straightforward, showing that a general solution of Eq. (23) has the following form:  $E_{\gamma,\omega}(z) = \mathcal{E}_{\gamma,\omega}(z) \exp(i\eta_{\gamma}z)$ , where  $\eta_{\gamma}^2 = \mu_0\omega^2\bar{\epsilon}_{\gamma\gamma}(\omega)$  with  $\gamma = a, b$ .  $\mathcal{E}_{\gamma,\omega}(z)$  is a function that is slowly varying compared to the factor  $\exp(i\eta_{\gamma}z)$ . The specific expression of  $\mathcal{E}_{\gamma,\omega}(z)$  is fixed by the boundary conditions.

Analogous to Eq. (23), the solution for Eq. (24) may be searched in the form  $E_{\gamma,2\omega}(z) = \mathcal{E}_{\gamma,2\omega}(z) \exp(ik_{\gamma}z)$  with  $k_{\gamma}^2 = (4\omega^2/c^2)\bar{\epsilon}_{\gamma\gamma}(2\omega)$ . However, in this case an exact solution cannot be found and we must apply the slowly varying envelope approximation (SVEA) [20].

Under SVEA, the solution for the field amplitude  $\mathcal{E}_{\gamma,2\omega}$  is given by

$$\begin{aligned} \mathcal{E}_{\gamma,2\omega}(d) &= id \frac{2\mu_0\omega^2}{k_{\gamma}} [T_{a\alpha\gamma}\mathcal{E}_{a,\omega}^2 + (T_{ab\gamma} + T_{ba\gamma})\mathcal{E}_{a,\omega}\mathcal{E}_{b,\omega} \\ &+ T_{bb\gamma}\mathcal{E}_{b,\omega}^2] e^{-ik_{\gamma}d}, \end{aligned} \quad (27)$$

where  $\mathcal{E}_{\gamma,2\omega}(d=0)$  has been set at zero and the following tensor has been introduced:

$$T_{\alpha\beta\gamma} = i\eta_{\beta}\bar{\Gamma}_{\gamma\alpha\beta}(\omega, \omega) e^{i\frac{(\eta_{\alpha} + \eta_{\beta} + k_{\gamma})d}{2}} \times \text{sync} \left[ (\eta_{\alpha} + \eta_{\beta} - k_{\gamma}) \frac{d}{2} \right], \quad (28)$$

(sync  $\equiv \sin(x)/x$ ).

Given the components of the optical field in the crystal-reference system, the optical field at the output of the sample in the laboratory frame may be found by projecting the fundamental beam vector  $\mathcal{E}_{\gamma,\omega}$  and the SH amplitude  $\mathcal{E}_{\gamma,2\omega}(d)$  on the axis  $\hat{x}$  and  $\hat{y}$ . It is useful to introduce the rotation matrix  $\mathbf{R}$ , defined by

$$\begin{pmatrix} \hat{a} \\ \hat{b} \end{pmatrix} = \mathbf{R} \begin{pmatrix} \hat{x} \\ \hat{y} \end{pmatrix} = \begin{pmatrix} \cos \vartheta & \sin \vartheta \\ -\sin \vartheta & \cos \vartheta \end{pmatrix} \begin{pmatrix} \hat{x} \\ \hat{y} \end{pmatrix}.$$

The SH optical field at the sample output in the laboratory frame is then given by

$$E_{j,2\omega}(d) = \sum_{\gamma=a,b} R_{j\gamma} \mathcal{E}_{\gamma,2\omega}(d) e^{ik_{\gamma}d}. \quad (29)$$

Inserting Eq. (27) in Eq. (29), we obtain

$$\begin{aligned} E_{j,2\omega}^{(h)}(d) &= i2d\mu_0\omega^2 \sum_h E_{h,\omega}^2 \sum_{\gamma=a,b} k_{\gamma}^{-1} R_{j\gamma} [T_{a\alpha\gamma} R_{ah}^{-1} R_{ah}^{-1} \\ &+ (T_{ab\gamma} + T_{ba\gamma}) R_{ah}^{-1} R_{bh}^{-1} + T_{bb\gamma} R_{bh}^{-1} R_{bh}^{-1}], \end{aligned} \quad (30)$$

where the index  $h = x, y$  refers to the input beam polarization, assumed to be linear.

The output SH intensity will have, in general, two components along the  $\hat{x}$  and  $\hat{y}$  axes, respectively. If the experimental setup is suitable for separately analyzing these two components, then four polarization combinations can be measured:  $xx, xy, yx, yy$ . The intensity of the SH component along the  $\hat{x}$  axis is proportional to  $|E_{x,2\omega}(d)|^2$ , whereas the intensity of the component along the  $\hat{y}$  axis is proportional to  $|E_{y,2\omega}(d)|^2$ . From Eq. (30), the following equations are found for the SH intensity  $S_{jh}(j, h = x, y)$  in the four polarization combinations:

$$\begin{aligned} S_{xx} &\propto |\mathcal{E}_{x,\omega}^2|^2 S_{\parallel}(\vartheta) \\ &= |\mathcal{E}_{x,\omega}^2|^2 \left| \frac{T_{aaa}}{k_a} \cos^3 \vartheta + \left( \frac{T_{aab}}{k_b} + \frac{T_{aba} + T_{baa}}{k_a} \right) \sin \vartheta \cos^2 \vartheta \right. \\ &\quad \left. + \left( \frac{T_{abb} + T_{bab} + T_{bba}}{k_b} + \frac{T_{bba}}{k_a} \right) \sin^2 \vartheta \cos \vartheta + \frac{T_{bbb}}{k_b} \sin^3 \vartheta \right|^2, \end{aligned} \quad (31)$$

$$\begin{aligned} S_{yx} &\propto |\mathcal{E}_{y,\omega}^2|^2 S_{\perp}(\vartheta) \\ &= |\mathcal{E}_{y,\omega}^2|^2 \left| \frac{T_{bba}}{k_a} \cos^3 \vartheta + \left( \frac{T_{bbb}}{k_b} - \frac{T_{aba} + T_{baa}}{k_a} \right) \sin \vartheta \cos^2 \vartheta \right. \\ &\quad \left. + \left( -\frac{T_{abb} + T_{bab} + T_{aaa}}{k_b} + \frac{T_{aaa}}{k_a} \right) \sin^2 \vartheta \cos \vartheta + \frac{T_{aab}}{k_b} \sin^3 \vartheta \right|^2, \end{aligned} \quad (32)$$

and from trivial arguments of symmetry

$$S_{yy} \propto |\mathcal{E}_{y,\omega}^2|^2 S_{\parallel}(\vartheta + \pi/2), \quad (33)$$

$$S_{xy} \propto |\mathcal{E}_{x,\omega}^2|^2 S_{\perp}(\vartheta + \pi/2). \quad (34)$$

### C. Nonlocal Second Harmonic Generation from Muscovite Mica

The general theory developed in the previous section is now applied to the specific case of a crystal of muscovite mica. Muscovite mica crystallizes in the monoclinic system; hence, it is optically biaxial. Let us indicate its principal dielectric axes with the unit vectors  $\hat{i}, \hat{j}$ , and  $\hat{k}$ , oriented as in Fig. 1. The principal dielectric axis  $\hat{k}$  forms an angle of  $\simeq 5^\circ$  with the laboratory  $\hat{z}$  axis [21]. The two principal axes  $\hat{i}$  and  $\hat{j}$  are almost parallel to the cleavage plane, which lies in the plane  $\hat{x}\hat{y}$  of the laboratory frame. This angle will be neglected in the following, and  $\hat{z}$  and  $\hat{k}$  will be considered almost parallel. Therefore, axes  $\hat{a}$  and  $\hat{b}$  introduced in the previous section are, with good approximation, coincident with the  $\hat{i}$  and  $\hat{j}$  axes.

If the refractive index along a given direction  $\gamma$  is defined as  $n_{\gamma,\omega} = \sqrt{\epsilon_{\gamma\gamma}(\omega)/\epsilon_0}$ , then the birefringence at  $\omega$  and  $2\omega$  may be written as  $\Delta_{\omega} = n_{b,\omega} - n_{a,\omega}$  and  $\Delta_{2\omega} = n_{b,2\omega} - n_{a,2\omega}$ , respectively. It is also useful to introduce the frequency dispersion with respect to axis  $\hat{a}$ ,  $\delta_a = n_{a,2\omega} - n_{a,\omega}$ . In the visible range,

the birefringence and dispersion of muscovite mica are of the order of  $5 \times 10^{-3}$  [22] and  $2 \times 10^{-2}$  [23], respectively.

Additionally mica possess a plane of symmetry, the so-called glide plane [24], orthogonal to the axis  $\hat{b}$ . The existence of a glide plane implies that all the elements of the tensor  $T_{\alpha\beta\gamma}$  containing an odd number of  $b$  indices vanish. Based on these assumptions, it is straightforward to demonstrate that  $S_{\parallel}(\vartheta)$  and  $S_{\perp}(\vartheta)$  can be put in the following forms that single out the  $\vartheta$  dependence of the SH intensity:

$$S_{\parallel}(\vartheta) \propto \cos^2 \vartheta [(A \cos^2 \vartheta + B)^2 + C], \quad (35)$$

$$S_{\perp}(\vartheta) \propto \cos^2 \vartheta [(A \cos^2 \vartheta + D)^2 + \mathcal{F}], \quad (36)$$

where we have introduced the following relations:

$$\mathcal{L} = \frac{T_{aaa} - T_{bba}}{k_a} - \frac{T_{abb} + T_{bab}}{k_b}, \quad (37)$$

$$\phi_a = \text{atan} \left[ \frac{\text{Im}(\mathcal{L})}{\text{Re}(\mathcal{L})} \right], \quad (38)$$

$$H_1 = \text{Re} \left[ \left( \frac{T_{bba}}{k_a} + \frac{T_{abb} + T_{bab}}{k_b} \right) e^{-i\phi_a} \right], \quad (39)$$

$$H_2 = \text{Re} \left[ \left( \frac{T_{abb} + T_{bab}}{k_b} - \frac{T_{aaa}}{k_a} \right) e^{-i\phi_a} \right], \quad (40)$$

$$A = |\mathcal{L}|, \quad (41)$$

$$B = \text{Re}(H_1), \quad (42)$$

$$C = [\text{Im}(H_1)]^2, \quad (43)$$

$$D = \text{Re}(H_2), \quad (44)$$

$$\mathcal{F} = [\text{Im}(H_2)]^2. \quad (45)$$

The new real constants  $A$ ,  $B$ ,  $C$ ,  $D$ , and  $\mathcal{F}$  are related to the old constants by the following implicit relations:

$$\sqrt{(A+B)^2 + C} = |T_{aaa}/k_a| = \left| \frac{\eta_a}{k_a} \right| |\Gamma_{aaa}| \text{sync} \left[ -\frac{\omega \delta_a d}{c} \right], \quad (46)$$

$$\sqrt{(A+D)^2 + \mathcal{F}} = |T_{bba}/k_a| = \left| \frac{\eta_b}{k_a} \right| |\Gamma_{abb}| \text{sync} \left[ \frac{\omega(\Delta_{\omega} - \delta_a) d}{c} \right], \quad (47)$$

$$\begin{aligned} \sqrt{(A+B+D)^2 + (\sqrt{C} \pm \sqrt{\mathcal{F}})^2} &= |(T_{abb} + T_{bab})/k_b| \\ &= \frac{|\eta_b \Gamma_{babz} + \eta_a \Gamma_{bbaz}|}{|k_b|} \times \text{sync} \left[ \frac{\omega \left( \frac{\Delta_{\omega}}{2} - \Delta_{2\omega} - \delta_a \right) d}{c} \right]. \end{aligned} \quad (48)$$

The sync functions entering in Eqs. (46)–(48) give a critical dependence of SHG on sample thickness in connection with sample birefringence.

This is clearly shown in Fig. 2, where the results of a simplified model developed in Appendix A are reported. In this figure, the  $S_{xx}$  signal as a function of  $\vartheta$  is shown for different sample thicknesses  $\tilde{d}$  (given in units of the fundamental wavelength). It is worth noting that the  $\vartheta$  functional form of  $S_{xx}$  varies dramatically, going from the thinnest to the thickest samples: in the thinnest samples, there are six, equally intense peaks, while for thicker samples, the diagrams display only two prominent peaks. It is also interesting to consider the dependence on thickness of the maximum value,  $S_{\text{max}}$ , of each SH diagram in  $\vartheta$ .  $S_{\text{max}}$  does not increase monotonically with thickness, but it shows strong oscillations. From Fig. 2 it is evident that a small variation in the sample thickness may lead to a strong suppression of SHG, even in the thickest samples. This is a clear signature of the effect of phase matching accounted by the sync functions.

### 3. EXPERIMENT

The experimental setup for SHG measurements in a transmission geometry is shown in Fig. 3. A mode-locked Nd:YAG laser generates pulses at a wavelength of 1064 nm, repetition rate of 10 Hz, and duration of 20 ps. The laser polarization is controlled using a combination of a cube polarizer and a half-wave plate. The laser beam impinging onto the mica at normal incidence is focused on the sample by means of a lens with 15 cm of focal length. For each sample, the cleavage plane is perpendicular to the beam propagation direction. A filter, F, stops the transmitted light of frequency  $\omega$  before detection, while the generated radiation of frequency  $2\omega$  is only slightly attenuated. The output polarization of the  $2\omega$  radiation is analyzed by means of a half-wave plate and a polarizing beam splitter. In order to further reduce any background light, the SH radiation passes through a monochromator. Finally, the SH photons are detected by means of a Hamamatsu R928S photomultiplier. The SHG has been analyzed for four mica disks of the highest quality, grade V-1 (SPI Supplies). The first two samples are freshly cleaved mica sheets of thickness 30 (sample M1) and 80  $\mu\text{m}$  (sample M2), respectively. The other two are mica disks, used as received from the supplier, with a

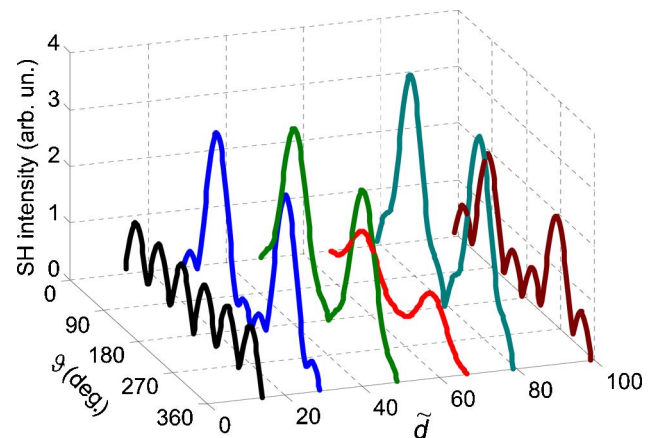


Fig. 2. (Color online) Results of the simplified model developed in Appendix A. The SH is plotted as a function of the azimuthal angle  $\vartheta$  and sample thickness  $\tilde{d}$  (in units of wavelength). Note the strong variability of the maximum SH intensity as a function of  $\tilde{d}$ .

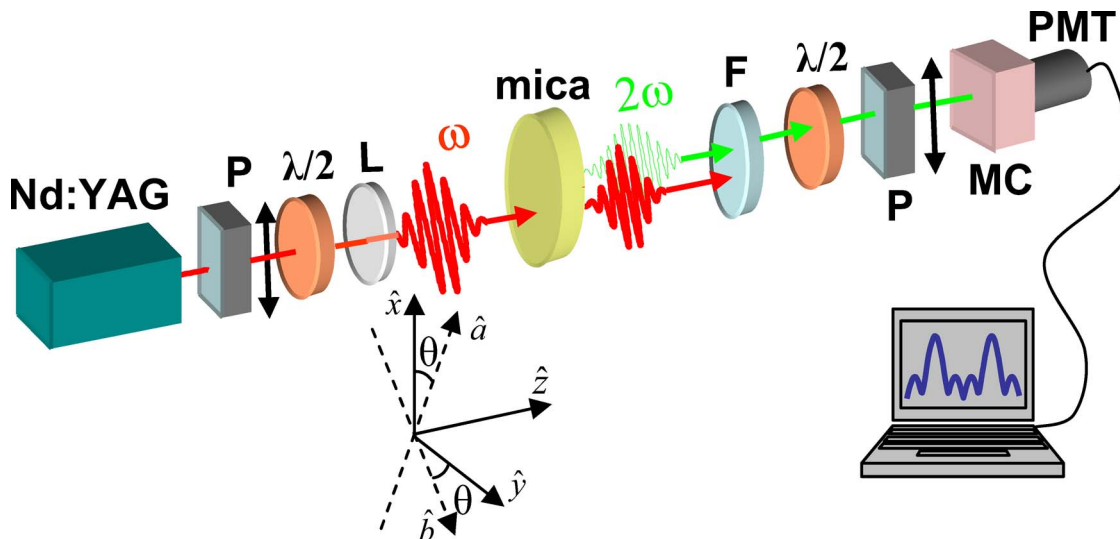


Fig. 3. (Color online) Layout of the experimental setup: P, Glan-Laser polarizer;  $\lambda/2$ , half-wave plate; L, lens; F, filter; MC, monochromator; and PMT, photomultiplier tube. For clarity, the fundamental and SH beams have been displaced, but in reality, they are collinear.

nominal thickness ranging from 275 to 325  $\mu\text{m}$  (samples M3 and M4). The SH signal has been measured as a function of the mica rotation around the normal to the cleavage plane for four different input-output polarization combinations:  $xx$ ,  $xy$ ,  $yy$ , and  $yx$ . According to the previous sections, the rotation angle around the normal to the crystal surface is indicated with  $\vartheta$  (see Figs. 1 and 3). All data have been taken at the same energy of the laser source (about 2.5 mJ per pulse on the sample) at room temperature (296 K).

#### 4. RESULTS AND DISCUSSION

The experimental results for the four samples are shown in Figs. 4–6. As an example, in Fig. 4, the diagrams with  $\vartheta$  dependence ( $\vartheta$  diagram) for sample M1 are reported for all four polarization combinations. Note that all four  $\vartheta$  diagrams display six approximately equal peaks. This is verified only in the thinnest sample. Within the experimental errors, the  $\vartheta$  diagram of  $S_{xx}$  is obtained from that of  $S_{yy}$  by simply rotating angle  $\vartheta$  by

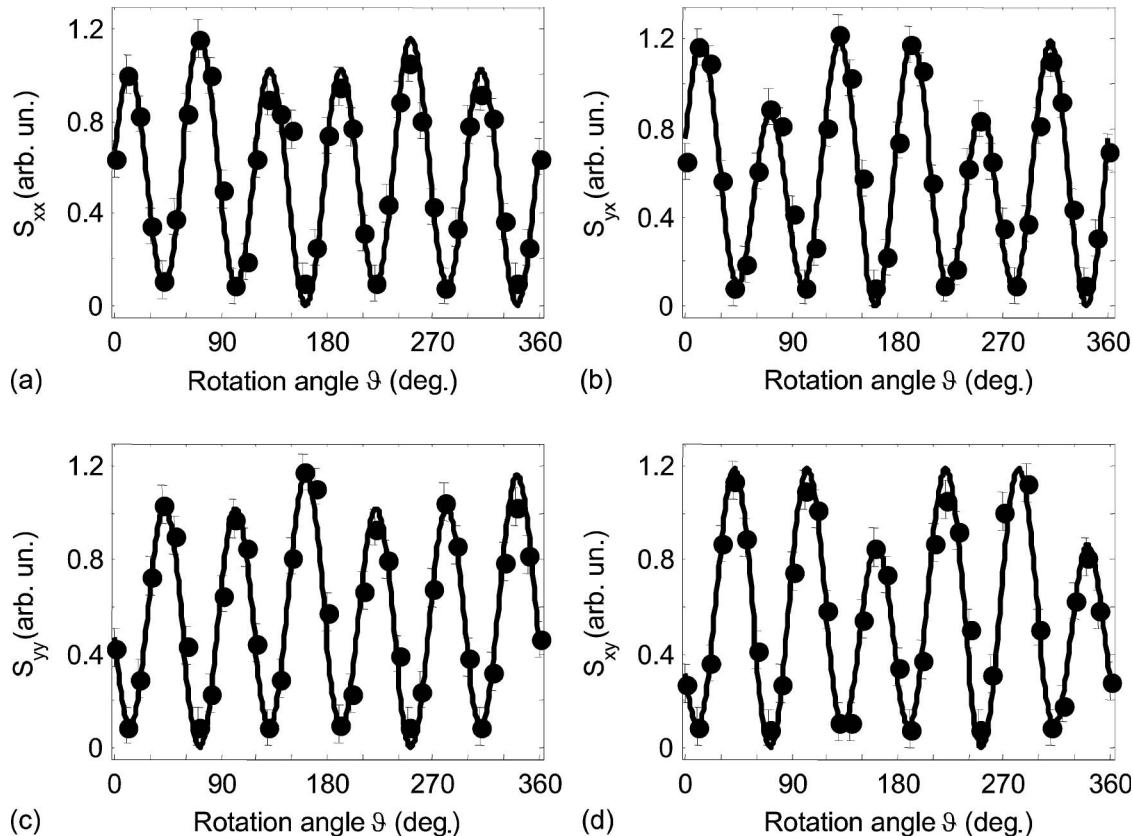


Fig. 4. SH signal of sample M1 for all polarization combinations. Error bars are given at a 90% level of confidence. The solid lines are the results of a best-fit procedure based on Eqs. (35) and (36). The four panels have the same units for the signal  $S$ .

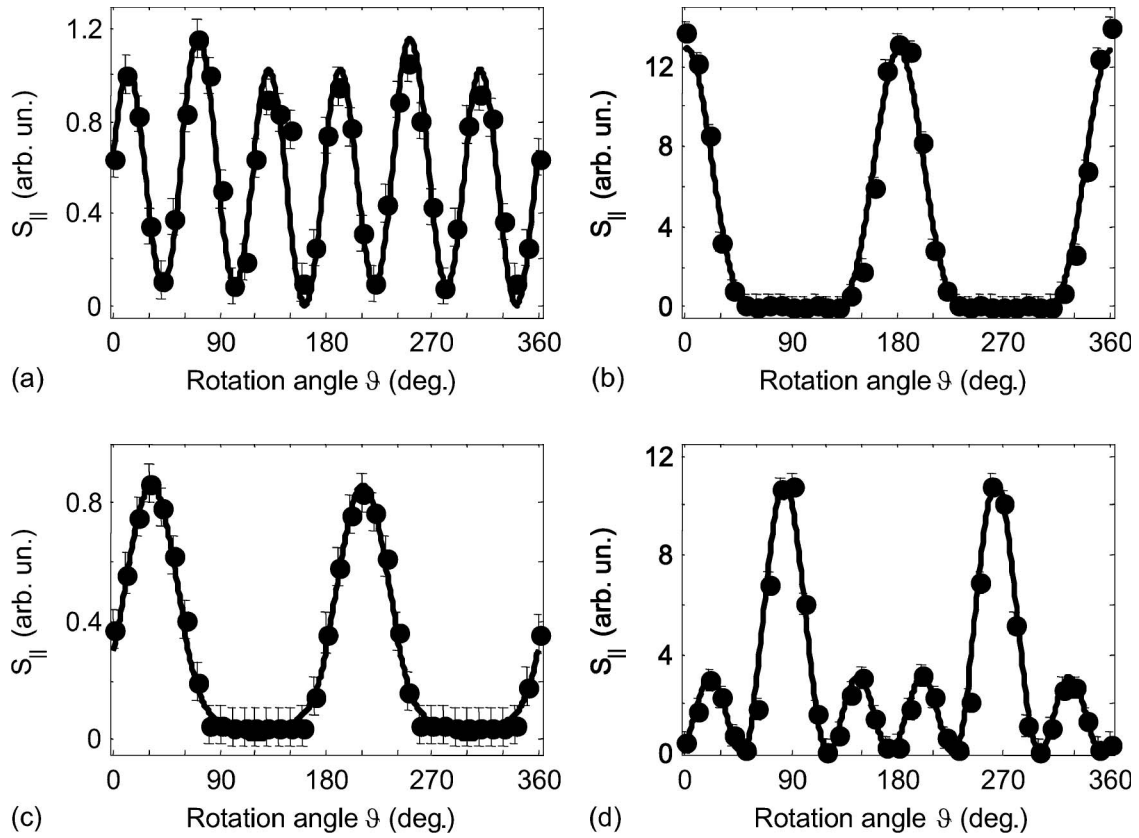


Fig. 5. Comparison of the SH signal of all the samples for the parallel polarization combinations: (a) M1, (b) M2, (c) M3, and (d) M4. Error bars and solid lines are the same as in the caption of Fig. 4. The four panels have the same units for the signal  $S$ .

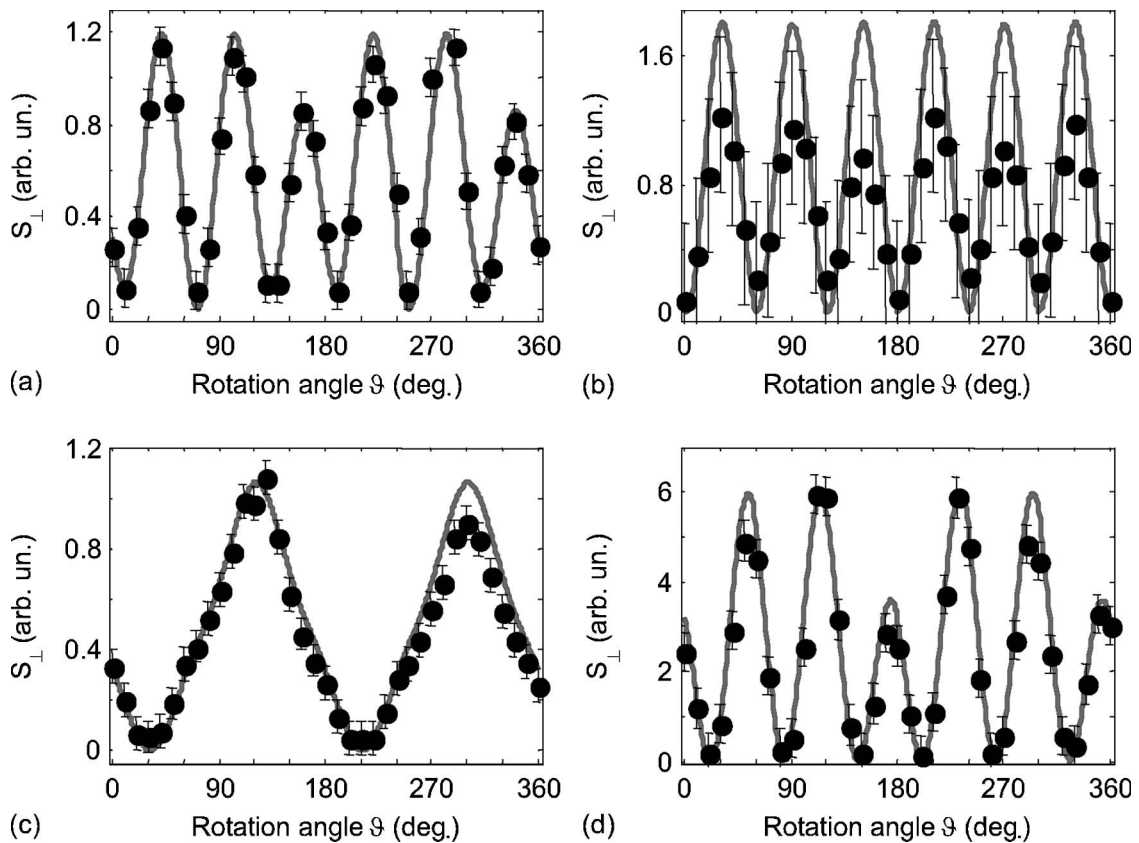


Fig. 6. Same comparison as in Fig. 5 but for the perpendicular polarization combinations.

**Table 1. Values of the Parameters Used for the Fitting Curves of Figs. 4–6<sup>a</sup>**

	$d$ ( $\mu\text{m}$ )	$\mathcal{A}$	$\mathcal{B}$	$\mathcal{C}$	$\mathcal{D}$	$\mathcal{F}$
M1	30	4.05	-3.01	-0.347	-3.17	0.369
M2	80	5.60	-1.90	-0	-4.20	0
M3	300	0.758	-0.177	0.338	-0.546	0.744
M4	300	-9.12	5.80	0	7.23	0.294

<sup>a</sup>In the second column, the sample thicknesses are reported.

90°, as expected. Similar relations are verified for all other samples as well (not shown).

Now we will focus the discussion on the parallel and perpendicular polarization combinations for all the samples. And so, in the following we will refer to the functions  $S_{\parallel}(\vartheta)$  and  $S_{\perp}(\vartheta)$ .

In Fig. 5 the  $\vartheta$  diagrams of  $S_{\parallel}$  for all four samples are compared. The comparison highlights a strong variability from sample to sample of both the  $\vartheta$  diagram shape and the maximum SH signal  $S_{\text{max}}$ . As already noted, the thinnest sample shows a characteristic  $\vartheta$  diagram with six peaks of approximately the same magnitude. The other samples give  $\vartheta$  diagrams with only two prominent peaks. Also,  $S_{\text{max}}$  varies drastically from sample to sample. The maximum SH intensity in sample M2 (80  $\mu\text{m}$  thickness) is 1 order of magnitude larger than in sample M1 [Figs. 5(b) and 5(a), respectively].  $S_{\text{max}}$  for sample M3 with a nominal thickness in the interval 275–325  $\mu\text{m}$  is of the same order of magnitude of sample M1 and, hence, 1 order of magnitude less than the thinner sample M2. In contrast,  $S_{\text{max}}$  for sample M4 [Fig. 5(d)], which has the same nominal thickness of M3, is 1 order of magnitude higher than M3 [Fig. 5(c)] and, hence, of the same order of magnitude as M2. In order to have an estimate of the absolute SH intensity generated in mica, we have compared the SH signal from sample M4 against the SH intensity from an  $x$ -cut quartz plate, 500  $\mu\text{m}$  thick, observed under the same experimental conditions. We have found that the SH intensity of the M4 sample is a factor  $9.4 \times 10^3$  lower than that of the reference quartz crystal.

In Fig. 6, the  $\vartheta$  diagrams of  $S_{\perp}$  for all the samples are reported. For this polarization combination, the  $\vartheta$  diagrams do not show the same behavior of the  $S_{\parallel}$  signal. Samples M1 and M2 display a  $\vartheta$  diagram with six peaks [Figs. 6(a) and 6(b), respectively]. The  $\vartheta$  diagram of M3 [Fig. 6(c)] shows two prominent peaks with a peculiar shape. Finally, the  $\vartheta$  diagram of M4 [Fig. 6(d)] shows four prominent peaks. In contrast to the parallel polarization combination,  $S_{\text{max}}$  also has a different behavior with thickness: all the samples, with the significant exception of M4, have a maximum SH intensity of the same order of magnitude.  $S_{\text{max}}$  of sample M4 is approximately five times larger.

Although with different trends for the two polarization combinations, the observed increase by approximately 1 order of magnitude of  $S_{\text{max}}$  from the thinnest to the thickest samples may only be explained by assuming that the SH signal is originated in the bulk of mica. Because mica samples are centrosymmetric, SHG must be caused by nonlocal higher order effects. Therefore, we have applied a best-fit procedure based on the theory developed in the previous sections in order to explain these experimental results (we also verified that a model considering only the surface local response of the SHG was not able to fit the experimental data). For each

sample, a global fit over all the polarization combinations is performed, letting free only the five parameters  $\mathcal{A}$ ,  $\mathcal{B}$ ,  $\mathcal{C}$ ,  $\mathcal{D}$ , and  $\mathcal{F}$ . The solid lines in Figs. 4–6 show the results of these fits. The agreement is excellent and further confirms our assumption that the observed SHG is nonlocal in nature. In Table 1 the fitted parameters are tabulated. These values may be inserted in Eqs. (46)–(48) for obtaining the  $\Gamma_{\text{afyz}}$  elements, but the sample birefringence and thickness must be known with high precision.

If the observed SHG originates in the bulk, it critically depends on phase-matching conditions and, hence, on the sample thickness, as predicted by the model presented in Fig. 2. This satisfactorily explains the strong suppression of SHG in sample M3, although the latter has a nominal thickness close to sample M4, where the SH signal is strong. The same argument explains the strong suppression of SHG in sample M2 for the perpendicular polarization combination, although this sample displays an efficient SHG for the parallel polarization combination. The different behavior of M2 for the two polarization combinations must be ascribed to the fact that the  $\Gamma_{\text{afyz}}$  elements add up differently in Eqs. (31) and (32), respectively.

Finally, we notice that the simpler six peak behavior of the thinnest sample of mica also leads to the relation  $3\Gamma_{\text{aaaz}} + \Gamma_{\text{babz}} + \Gamma_{\text{abbz}} + \Gamma_{\text{bbaz}} \simeq 0$ , as shown in Appendix A.

## 5. CONCLUSIONS

In this paper, a detailed investigation of SHG from muscovite mica in a transmission normal-incidence geometry has been reported. Samples with different thicknesses have been studied, and a strong dependence of SHG on sample thickness has been found. In particular, a strong enhancement of the SH signal for some of the thickest samples has been observed. The SH signal does not increase monotonically with thickness, but it is found instead to be erratic in nature, with dramatic variations between samples that have the same nominal thickness.

This extreme variability of SHG intensity with thickness can be only explained by assuming that SHG originates in the volume of mica. Because mica is a centrosymmetric crystal, SHG must be ascribed to nonlocal higher order contributions to the material nonlinear polarization.

Based on this hypothesis, we have developed a detailed theoretical model including nonlocal higher order terms and crystal anisotropy. Our theoretical analysis is actually independent of the specific case of mica, and it is applicable to any centrosymmetric birefringent crystals. As explained in Section 1, a general theory describing nonlocal SHG in birefringent centrosymmetric crystals and in a transmission geometry has never been reported in literature.

This model has been used for fitting the experimental data. We find excellent agreement between data and fits. In particular, the model was able to explain the large differences of the maximum SH intensity observed in samples M3 and M4 that nominally have the same thickness (275–325  $\mu\text{m}$ ). According to our theoretical analysis, the extreme variability of  $S_{\text{max}}$  is caused by optical phase matching in connection with mica birefringence.

The experimental and theoretical results of this work clearly show that care is needed when using mica as the substrate for SHG experiments in a transmission geometry because, in some conditions, a large substrate background

signal may be generated. At the same time, the analysis presented here shows that a reduction of the SH signal from the bulk of mica is possible by using a suitable combination of sample thickness and azimuthal  $\vartheta$  angle.

Finally, we point out that in the present work, we have not investigated the dependence of the SH signal on the incidence angle. This test can be useful to further confirm our interpretation based on the nonlocal second-order nonlinear response of centrosymmetric crystals. In particular, this experiment is expected to highlight interference effects analogous to the SH fringes observed in noncentrosymmetric crystals by Maker *et al.* [25], but with some deviation due to the additional dependence on the  $\mathbf{k}$  vector. This experiment will be the subject of future work.

## APPENDIX A: SIMPLE MODEL FOR SECOND HARMONIC INTENSITY

In this appendix, a simple model for SH intensity is derived. The starting point is Eq. (31), and, hence, the model will provide us with a simplified expression for the signal  $S_{xx}$  alone. However, note that the assumptions used in the following are too rough for describing quantitatively the differences between the different polarization combinations. Therefore, this model can be only used for understanding qualitatively the dependence on thickness and  $\vartheta$  of the SH intensity, independently of the specific polarization combination.

Equation (31) may be rewritten so as to make evident the dependence on the sync functions that account for the optical phase-matching effects:

$$S_{xx} \propto |[\Gamma_{aaaz}f_0(\tilde{d}) - \Gamma_{abbz}f_1(\tilde{d}) - (\Gamma_{babz} + \Gamma_{bbaz})f_2(\tilde{d})] \cos^3 \vartheta + \Gamma_{abbz}f_1(\tilde{d}) \cos \vartheta + (\Gamma_{babz} + \Gamma_{bbaz})f_2(\tilde{d}) \cos \vartheta|^2, \quad (\text{A1})$$

where  $\tilde{d} = d/\lambda$  ( $\lambda$  is the wavelength of the fundamental beam in the vacuum) and

$$f_0(\tilde{d}) = \text{sinc}(-2\pi\delta_a\tilde{d}), \quad (\text{A2})$$

$$f_1(\tilde{d}) = \text{sinc}[2\pi(\Delta_\omega - \delta_a)\tilde{d}], \quad (\text{A3})$$

$$f_2(\tilde{d}) = e^{-i\pi\Delta_\omega\tilde{d}} \times \text{sinc}[2\pi(\Delta_\omega/2 - \Delta_{2\omega} - \delta_a)\tilde{d}]. \quad (\text{A4})$$

In the limit of small thickness, Eq. (A1) reads

$$S_{xx} \propto \frac{1}{16} \left| (\Gamma_{aaaz} - \Gamma_{abbz} - \Gamma_{babz} - \Gamma_{bbaz}) \cos(3\vartheta) + (3\Gamma_{aaaz} + \Gamma_{abbz} + \Gamma_{babz} + \Gamma_{bbaz}) \cos \vartheta \right|^2, \quad (\text{A5})$$

where the trigonometric relation  $\cos^3 \vartheta = (1/4) \cos(3\vartheta) + (3/4) \cos \vartheta$  has been used.

Experimentally, it turns out that for small thicknesses, the dependence on  $\vartheta$  is approximately proportional to the square of the  $\cos(3\vartheta)$  function. Therefore, the following relation should hold true with good approximation:  $\Gamma_{babz} + \Gamma_{bbaz} = -3\Gamma_{aaaz} - \Gamma_{abbz}$ . Note that the  $\Gamma_{\alpha\beta\gamma z}$  are intrinsic properties of the material that do not depend on the thickness. Therefore,

the latter relation may be used for simplifying Eq. (A1) into the following expression:

$$S_{xx} \propto \cos^2 \vartheta \{ [f_0(\tilde{d}) + 3f_2(\tilde{d})] \Gamma_{aaaz} + [f_2(\tilde{d}) - f_1(\tilde{d})] \Gamma_{abbz} \} \cos^2 \vartheta - 3f_2(\tilde{d}) \Gamma_{aaaz} - [f_2(\tilde{d}) - f_1(\tilde{d})] \Gamma_{abbz}^2. \quad (\text{A6})$$

As seen above, the dispersion in mica is at least 1 order of magnitude larger than the birefringence. Therefore, in Eqs. (A2)–(A4), the denominators of the sync functions may be approximated to  $-2\pi\delta_a\tilde{d}$  and factorized, leading to the following simplified equation approximately valid for mica:

$$S_{xx} \propto \left| \left[ \frac{\Gamma_{aaaz}}{\Gamma_{abbz}} g_0(\tilde{d}) + g_1(\tilde{d}) \right] \cos^2 \vartheta - \frac{\Gamma_{aaaz}}{\Gamma_{abbz}} g_2(\tilde{d}) - g_1(\tilde{d}) \right|^2, \quad (\text{A7})$$

where

$$g_0(\tilde{d}) = \sin(-2\pi\delta_a\tilde{d}) + 3e^{-i\pi\Delta_\omega\tilde{d}} \sin[2\pi(\Delta_\omega/2 - \Delta_{2\omega} - \delta_a)], \quad (\text{A8})$$

$$g_1(\tilde{d}) = e^{-i\pi\Delta_\omega\tilde{d}} \sin[2\pi(\Delta_\omega/2 - \Delta_{2\omega} - \delta_a)] - \sin[2\pi(\Delta_\omega - \delta_a)\tilde{d}], \quad (\text{A9})$$

$$g_2(\tilde{d}) = g_0(\tilde{d}) - \sin(-2\pi\delta_a\tilde{d}). \quad (\text{A10})$$

Equation (A7) may be used to draw the graph shown in Fig. 2. The latter has been obtained by assuming the ratio of  $\Gamma_{aaaz}/\Gamma_{abbz}$  being equal to one.

## REFERENCES AND NOTES

1. H. Yang, A. Kuperman, N. Coombs, S. Mamiche-Afara, and G. A. Ozin, "Synthesis of oriented films of mesoporous silica on mica," *Nature* **379**, 703–705 (1996).
2. W. H. Briscoe, S. Timtuss, F. Tiberger, R. K. Thomas, D. J. McGillivray, and J. Klein, "Boundary lubrication under water," *Nature* **444**, 191–194 (2006).
3. M. Qin, L. K. Wang, and X. Z. Feng, "Bioactive surface modification of mica and poly(dimethylsiloxane) with hydrophobins for protein immobilization," *Langmuir* **23**, 4465–4471 (2007).
4. B. Zappone, M. Ruths, G. W. Greene, G. D. Jay, and J. N. Israelachvili, "Adsorption lubrication, and wear of lubricin on model surfaces: polymer brush-like behavior of a glycoprotein," *Biophys. J.* **92**, 1693–1708 (2007).
5. O. Agam, "Viscous fingering in volatile thin films," *Phys. Rev. E* **79**, 021603 (2009).
6. T. Fukuma, Y. Ueda, S. Yoshioka, and H. Asakawa, "Atomic-scale distribution of water molecules at the mica-water interface visualized by three-dimensional scanning force microscopy," *Phys. Rev. Lett.* **104**, 016101 (2010).
7. Y. R. Shen, "Surface-properties probed by second-harmonic and sum-frequency generation," *Nature* **337**, 519–525 (1989).
8. Y. R. Shen, "Surfaces probed by nonlinear optics," *Surf. Sci.* **299**, 551–562 (1994).
9. X. Zhuang, L. Marrucci, and Y. R. Shen, "Surface-monolayer-induced bulk alignment of liquid crystals," *Phys. Rev. Lett.* **73**, 1513–1516 (1994).
10. X. Zhuang, D. Wilk, L. Marrucci, and Y. R. Shen, "Orientation of amphiphilic molecules on polar substrates," *Phys. Rev. Lett.* **75**, 2144–2147 (1995).
11. L. Marrucci, D. Paparo, G. Cerrone, C. de Lisio, E. Santamato, S. Solimeno, S. Ardizzone, and P. G. Quagliotto, "Probing interfacial properties by optical second-harmonic generation," *Opt. Lasers Eng.* **37**, 601–610 (2002).

12. A. Savoia, D. Paparo, P. Perna, Z. Ristic, M. Salluzzo, F. Miletto Granozio, U. Scotti di Uccio, C. Richter, S. Thiel, J. Mannhart, and L. Marrucci, "Polar catastrophe and electronic reconstructions at the  $\text{LaAlO}_3/\text{SrTiO}_3$  interface: evidence from optical second harmonic generation," *Phys. Rev. B* **80**, 075110 (2009).
13. P. Guyot-Sionnest, W. Chen, and Y. R. Shen, "General considerations on optical second-harmonic generation from surfaces and interfaces," *Phys. Rev. B* **33**, 8254–8263 (1986).
14. J. E. Sipe, D. J. Moss, and H. M. van Driel, "Phenomenological theory of optical second- and third-harmonic generation from cubic centrosymmetric crystals," *Phys. Rev. B* **35**, 1129–1141 (1987).
15. X. Wei, S.-C. Hong, A. I. Lvovsky, H. Held, and Y. R. Shen, "Evaluation of surface vs bulk contributions in sum-frequency vibrational spectroscopy using reflection and transmission geometries," *J. Phys. Chem. B* **104**, 3349–3354 (2000).
16. B. Jérôme and Y. R. Shen, "Anchoring of nematic liquid-crystals on mica in the presence of volatile molecules," *Phys. Rev. E* **48**, 4556–4574 (1993).
17. G. Berkovic, "New studies of liquid and solid surfaces using second harmonic generation," *Phys. A* **168**, 140–148 (1990).
18. R. Yerushalmi-Rozen, J. Klein, and G. Berkovic, "*In situ* probing of polymer grafting from solution onto solid substrates by non-linear optics," *Langmuir* **8**, 1392–1397 (1992).
19. M. Omote, H. Kitaoka, E. Kobayashi, O. Suzuki, K. Aratake, H. Sano, G. Mizutani, W. Wolf, and R. Podloucky, "Spectral, tensor, and *ab initio* theoretical analysis of optical second harmonic generation from the rutile  $\text{TiO}_2$  (110) and (001) faces," *J. Phys. Condens. Matter* **17**, S175–S200 (2005).
20. A. Yariv, *Quantum Electronics* (Wiley, 1989).
21. M. Medhat and S. Y. El-Zaiat, "Interferometric determination of the birefringence dispersion of anisotropic materials," *Opt. Commun.* **141**, 145–149 (1997).
22. B. Gauthier-Manuel, "Simultaneous determination of the thickness and optical constants of weakly absorbing thin films," *Meas. Sci. Technol.* **9**, 485–487 (1998).
23. A. I. Bailey and S. M. Kay, "Measurement of refractive index and dispersion of mica, employing multiple beam interference techniques," *Br. J. Appl. Phys.* **16**, 39–46 (1965).
24. In crystallography, the glide plane indicates a symmetry operation describing how a reflection in a plane, followed by a translation parallel to that plane, may leave the crystal unchanged [26]. Note that the tensors characterizing the optical response are not dependent on the translations.
25. P. D. Maker, R. W. Terhune, M. Nisenoff, and C. M. Savage, "Effects of dispersion and focusing on the production of optical harmonics," *Phys. Rev. Lett.* **8**, 21–22 (1962).
26. W. Borchardt-Ott, *Crystallography* (Springer-Verlag, 1995).